Robotica (2014) volume 32, pp. 571–589. © Cambridge University Press 2013
doi:10.1017/S026357471300088X

A new kinematics method based on a dynamic visual window for a surgical robot

Lingtao Yu†,‡, Zhengyu Wang†*, Peng Yu†, Tao Wang†, Huajian Song† and Zhijiang Du‡

† *College of Mechanical and Electrical Engineering, Harbin Engineering University, Harbin 150001, P. R. China*
‡*State Key Laboratory of Robotics and System (HIT), Harbin Institute of Technology, Harbin 150080, P. R. China*

(Accepted August 2, 2013. First published online: September 4, 2013)

SUMMARY
This paper proposes a new effective kinematics method based on the dynamic visual window (DVW) for a surgical robot that is equipped with two instrument arms and one laparoscope arm, to enable doctors to achieve operations with their visual habits under the laparoscopic visual environment. The problem of the consistency principle between the doctor's operations under the visual window's feedback and the master–slave operations of the surgical robot is solved. The kinematics models of the surgical robotic arms are established, and the new kinematics methods based on the DVW of the laparoscope and instrument arms are proposed according to their inverse kinematics with respect to the visual coordinate system. Finally, the proposed kinematics method is verified by simulation experiments based on the theoretical algorithm and the mechanism model; the multiple sets of the simulation data are presented to illustrate the correctness and feasibility of the new method in this research.

KEYWORDS: Robotics; Surgical robot; Kinematics; Dynamic visual window; Simulations.

1. Introduction

The minimally invasive surgery (MIS) has been used more and more extensively with the development of the laparoscopic surgical robotic system (LSRS) and changed the way we perceive and practice surgery,[1] due to all the changes that robotic surgery has made in the way of performing, teaching and practicing surgery.[2] The structure and function developments of the LSRS are as man–machine integrated as possible and suitable for doctors' demands in the operation. In addition, it is significant to establish the effective kinematics method for the LSRS, so as to make doctors accustomed to undergo surgical operations.

The most well-known commercialized systems are the Zeus and the da Vinci robots,[3,4,5] and the da Vinci system has been the most widely used surgical robot in the MIS. The DLR MIRO system[6,7] is a new versatile lightweight robot for surgical applications, which focuses on compact, slim and lightweight design to assist the surgeon directly at the operating table without interference. The Raven system[8,9] was developed at the University of California at Santa Cruz and the University of Washington and modelled on a system originally designed for military use.[10] Researchers of the Technical University of Eindhoven have developed the Surgeon's Operating Force feedback Interface Eindhoven called SOFIE.[11] The University of Hawaii-Manoa has built a simple, low-cost, modular system for performing laparoscopic surgery.[12]

The improvements of the LSRS are not only in developing its structure and function but also in establishing preferable kinematics algorithms for its slave manipulators, so that doctors can use the LSRS to finish the MIS with comfortable operations.

* Corresponding author. E-mail: flyman@hrbeu.edu.cn

https://doi.org/10.1017/S026357471300088X Published online by Cambridge University Press

There is a prototype robotic system for the MIS, which has two instrument arms, an autonomous robotic camera assistant and two haptic devices to control the instrument arms.[13] They developed a prediction method based on the Markov model and interference model and trajectory clustering to predict states for the autonomous guidance of the endoscopic camera. And using long-term prediction of the instruments' movement can improve the positioning of the endoscope. However, the complexity of trajectories of laparoscopic interventions represents a significant obstacle for the robust prediction of the ongoing intervention. Evaluations on a phantom showed a hit rate varying between 89.1% and 92.3% in predicting the end-effector's motion.

A new LSRS called ceiling mounted robots with surgical instruments[14] has been developed. The approach utilizes both encoder readings and visual information, in order to stabilize tracking in image space. As tracking modality they utilize the contracting curve density algorithm that looks for maximal separation of local colour statistics along the contour of a model. However, in regions with the very dark background, the greyish shaft cannot be separated correctly and tracking is lost.

Stephen[15] developed the HARP surgical robot and presented a filtering method for estimating the shape and end-effector's position and orientation (PAO) of a highly articulated surgical snake robot that can create a more accurate and representative 3D-rendered visualization for image-guided surgery. However, in the case of a cardiac experiment, it is worth noting that if the robot is interacting with deformable tissue and/or moving tissue, the estimation of shape can be adversely affected. And more advanced models are required based on the real celiac environment.

The Technical University of Cluj-Napoca has developed the PARASURG 5M hybrid parallel robot; Bogdan[16] proposed a new inverse dynamic model that was obtained using the virtual work method on the basis of dynamically equivalent lumped masses. The method proved to be more efficient because it can eliminate all forces and internal joints and allows direct determination of forces/torques of the robot for given laws of motion for the end effector. Oscar[17] illustrated how intraoperative navigation based on optical tracking of a fluorescence endoscope may help to further improve the accuracy of hybrid surgical guidance.

The matched kinematics method for each LSRS has its own characteristics, because of the different robotic structure and function in their dedicated surgical technique. Therefore, the research on the kinematics method based on the DVW is important in theories and practical applications, especially for the surgical robot equipped with instrument and laparoscope arms. This paper proposes a new kinematics method for the instruments and laparoscope arms, aiming at being suitable for doctors' visual sense and operation habits during the surgery; it can solve the problem of the consistency principle between the doctor's operations under the visual feedback of 3D visual window and the master–slave operations of the LSRS. Meanwhile, the kinematics algorithms can be the specialized kinematics method for this kind of LSRS and other applicative robotics industry.

2. Problem Statement

2.1. Kinematics method of the laparoscope arm

The laparoscopic visual window consists of the current visual window and the objective visual window. During the surgical procedure, if the current visual window cannot satisfy the doctors' demand, the visual window needs to be moved left/right, up/down and forward/back; these motions are with respect to the current visual window. The doctors use the master manipulator to control the laparoscope arm's position for achieving the expected visual field, which is defined as the objective visual window. The three types of motion for the 3D visual window are shown in Fig. 1, which move along the axis x, y, z of the laparoscope's visual coordinate system. The visual window's replacement process is a result of the 3D dynamic movement; if the three types of motion and the master–slave manipulation of the LSRS are consistent, it is conducive to the doctors' operation for achieving the optimum visual feedback from the abdomen. The new kinematics method based on the DVW of the laparoscope arm is established according to its inverse kinematics with respect to the laparoscope arm's visual coordinate system. Therefore, we can calculate the motion state of the 3D visual window through the laparoscope arm's kinematics algorithm proposed in this study.

https://doi.org/10.1017/S026357471300088X Published online by Cambridge University Press

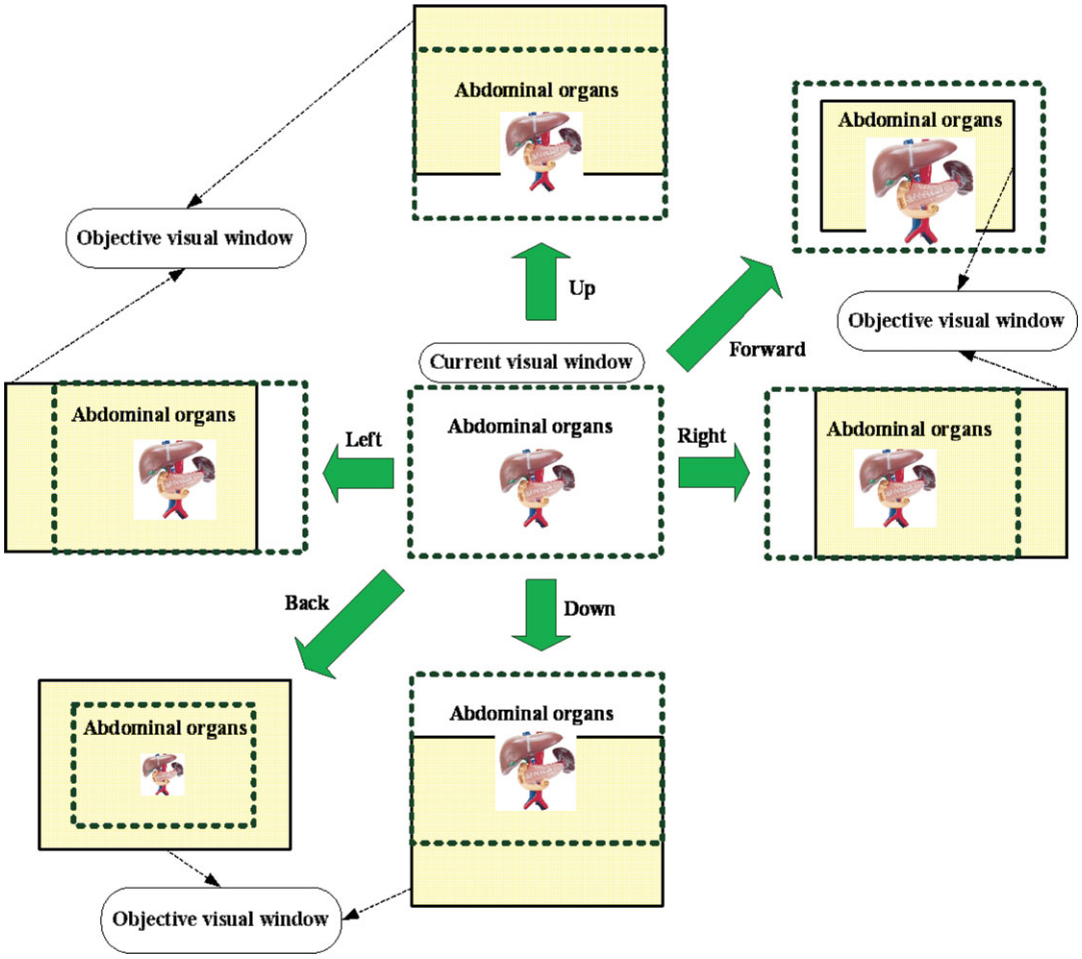


Fig 1. (Colour online) The objective 3D visual window based on DVW.

2.2. Kinematics method of the instrument arm

If the objective visual window is ready for the doctors' demand, the current visual window will be replaced by the objective visual window and the laparoscope's visual coordinate system is changed; this is a 3D dynamic replacement process during the surgical procedure. The doctors use the master manipulators to control the instrument arms' PAO for the desired operations with the visual window's visual feedback. If the devices' motion of the instrument arms in the 3D visual window and the master–slave manipulation of the LSRS are consistent, it can be suitable for the doctors' visual and operation habits. As shown in Fig. 2, i.e. the current PAO of the instrument arms' devices with respect to the 3D visual window, the new kinematics method based on the DVW of the instrument arm is established according to its inverse kinematics with respect to the laparoscope arm's visual coordinate system, and their objective PAO can be calculated through the instrument arm's kinematics algorithm proposed in this research.

3. Normalization of the Base Coordinate System

This research keeps attention on the LSRS, which consists of two instrument arms and one laparoscope arm in-between position of them. For convenience sake, we build the base coordinate system (BCS) on the laparoscope arm as the normalized BCS. Therefore, we need to complete the transformation between instrument arms and normalized BCS. As shown in Fig. 3, these are the relative location relations among the three arms' BCSs according to the structure of the LSRS. The coordinate

https://doi.org/10.1017/S026357471300088X Published online by Cambridge University Press

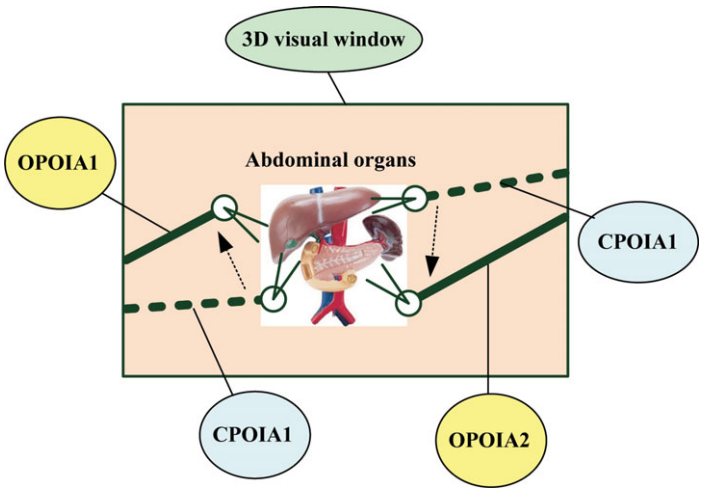


Fig. 2. (Colour online) The objective instrument arms' devices based on DVW. The OPOIA represents the objective position and orientation of the instrument arm and the CPOIA represents the current position and orientation of the instrument arm.

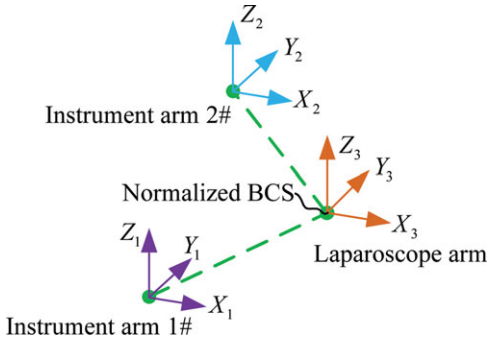


Fig. 3. (Colour online) The position relations of the three arms' BCSs.

transformation from the normalized BCS to the instrument arms is given by Eq. (1):

$$ {}^{\mathrm{B}}_{\mathrm{dev}}\boldsymbol{T}_{\lambda} = \begin{bmatrix} 1 & 0 & 0 & k_{\lambda} \\ 0 & 1 & 0 & k_3 \\ 0 & 0 & 1 & 0 \\ 0 & 0 & 0 & 1 \end{bmatrix}, \tag{1} $$

where k_{λ} and k_3 represent the position constant of each instrument arm. When $\lambda = 1$, ${}^{\mathrm{B}}_{\mathrm{dev}}\boldsymbol{T}_1$ represents the coordinate transformation from the normalized BCS to the instrument arm 1. When $\lambda = 2$, ${}^{\mathrm{B}}_{\mathrm{dev}}\boldsymbol{T}_2$ represents the coordinate transformation from the normalized BCS to the instrument arm 2.

4. The Kinematics Algorithm Based on DVW for the Laparoscope Arm

Describing the algorithm in kinematics is equal to moving the 3D visual window through the positive and negative directions of the laparoscope arm's tool coordinate system (TCS). Therefore, we analyse the kinematics model and establish its kinematics algorithm based on the DVW.

4.1. Kinematical modelling of the laparoscope arm

The first four arm joints of the LSRS are passive structures and the surgery assistant places them in the optimal position before the surgery. Then, the passive joints are fixed by electromagnetic clutches and the system collects the data of each joint by its encoder for the basic information inputting to the kinematics algorithm.

https://doi.org/10.1017/S026357471300088X Published online by Cambridge University Press

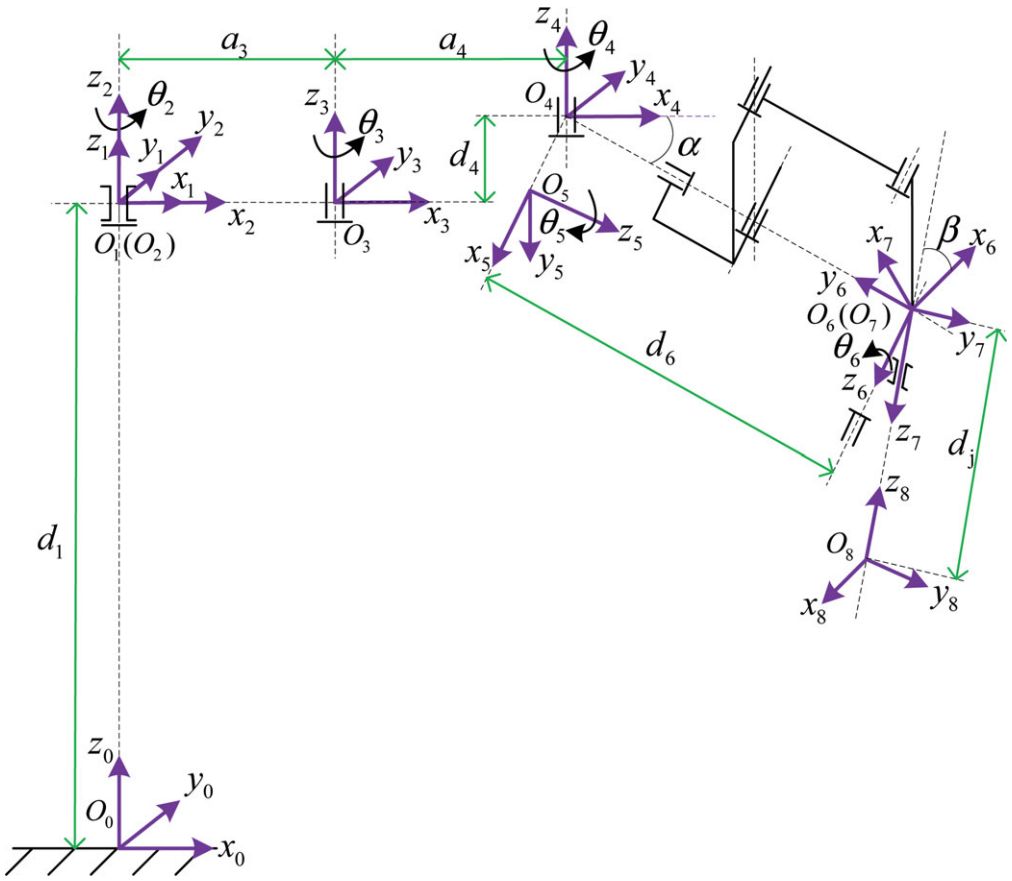


Fig. 4. (Colour online) The kinematics coordinate systems of the laparoscope arm.

According to the laparoscope arm's structural features, the kinematics coordinate systems are established as shown in Fig. 4. And the frame ${}_{\text{lap}}O_0$ is the normalized BCS, the frames ${}_{\text{lap}}O_1, {}_{\text{lap}}O_2, {}_{\text{lap}}O_3, {}_{\text{lap}}O_4$ are the first four passive joints' coordinate systems, the frame ${}_{\text{lap}}O_8$ is the TCS, and the frames ${}_{\text{lap}}O_5$, ${}_{\text{lap}}O_6$, ${}_{\text{lap}}O_7$ are the other joints' coordinate systems.

The coordinate transformation from the frame ${}_{\text{lap}}O_0$to${}_{\text{lap}}O_4$ is given by Eq. (2):

$$ {}^{0}_{4}\boldsymbol{T}_{\text{pas}} = {}^{0}_{1}\boldsymbol{T}_{\text{pas}} \cdot {}^{1}_{2}\boldsymbol{T}_{\text{pas}} \cdot {}^{2}_{3}\boldsymbol{T}_{\text{pas}} \cdot {}^{3}_{4}\boldsymbol{T}_{\text{pas}}. \tag{2} $$

Matrix ${}^{0}_{4}\boldsymbol{T}_{\text{pas}}$ is calculated by the basic data and information of the passive joints' encoders, which is a constant matrix. According to robotics, it is simple to calculate matrices ${}^{4}_{5}\boldsymbol{T}_{\text{pas}}$, ${}^{5}_{6}\boldsymbol{T}_{\text{pas}}$, ${}^{6}_{7}\boldsymbol{T}_{\text{pas}}$ and ${}^{7}_{8}\mathbf{T}_{\text{pas}}$, which are the neighbouring coordinate transformation among the frames ${}_{\text{lap}}O_4$, ${}_{\text{lap}}O_5$, ${}_{\text{lap}}O_6$, ${}_{\text{lap}}O_8$.

With the above parameters known, the forward kinematics' coordinate transformation from the normalized BCS ${}_{\text{lap}}O_0$ to the TCS ${}_{\text{lap}}O_8$ is given by Eq. (3):

$$ {}^{\text{B}}_{8}\boldsymbol{T}_{\text{lap}} = {}^{0}_{8}\boldsymbol{T}_{\text{lap}} = {}^{0}_{4}\boldsymbol{T}_{\text{pas}} \cdot {}^{4}_{5}\boldsymbol{T}_{\text{lap}} \cdot {}^{5}_{6}\boldsymbol{T}_{\text{lap}} \cdot {}^{6}_{7}\boldsymbol{T}_{\text{lap}} \cdot {}^{7}_{8}\boldsymbol{T}_{\text{lap}} = \begin{bmatrix} {}_{\text{lap}}n_x & {}_{\text{lap}}o_x & {}_{\text{lap}}a_x & {}_{\text{lap}}p_x \\ {}_{\text{lap}}n_y & {}_{\text{lap}}o_y & {}_{\text{lap}}a_y & {}_{\text{lap}}p_y \\ {}_{\text{lap}}n_z & {}_{\text{lap}}o_z & {}_{\text{lap}}a_z & {}_{\text{lap}}p_z \\ 0 & 0 & 0 & 1 \end{bmatrix}, \tag{3} $$

where

$$ {}_{\text{lap}}n_x = c_5 s_{2+3+4} - s_\alpha s_5 c_{2+3+4}, $$

$$ {}_{\text{lap}}n_y = -c_5 c_{2+3+4} - s_\alpha s_5 s_{2+3+4}, $$

https://doi.org/10.1017/S026357471300088X Published online by Cambridge University Press

$$
\begin{aligned}
{}_{\text{lap}}n_z &= -c_\alpha s_5,\\
&\cdots\cdots\\
{}_{\text{lap}}p_x &= a_3c_2 + a_4c_{2+3} + d_6c_\alpha c_{2+3+4} + (d_{\text{j}}c_{6-\beta} + d_7c_{6+\beta})(c_\alpha c_{2+3+4} + c_5s_\alpha c_{2+3+4} - s_5s_{2+3+4}),\\
{}_{\text{lap}}p_y &= a_3s_2 + a_4c_{3-2} + d_6c_\alpha c_{3-2-4} + (d_{\text{j}} + d_7)(s_5c_{6-\beta}s_{3-2-4} + s_{6-\beta}c_\alpha c_{3-2-4} - c_5s_\alpha c_{6-\beta}c_{3-2-4}),\\
{}_{\text{lap}}p_z &= d_1 + d_4 - d_6s_\alpha + (d_{\text{j}} + d_7)(s_{\beta-6}s_\alpha - s_{\beta+\alpha}c_5c_6),
\end{aligned}
$$

where c and s represent cos and sin, c_{2+3+4} and s_{2+3+4} represent cos $(\theta_2+\theta_3+\theta_4)$ and sin $(\theta_2+\theta_3+\theta_4)$, which are the same in the following equations.

There are only three active joints driven by servo motors for controlling the laparoscope's position, so their inverse kinematics is calculated based on the fourth passive joint's frame ${}_{\text{lap}}O_4$. In order to simplify the calculation, we try to roll the frame ${}_{\text{lap}}O_4$ along its axis y_4 for $(\alpha + 90^\circ)$ as a new frame ${}_{\text{lap}}O'_4$, and the coordinate transformation ${}^4_8\boldsymbol{T}'_{\text{lap}}$ from the frame ${}_{\text{lap}}O'_4$ to ${}_{\text{lap}}O_8$ is given by Eq. (4):

$$
\begin{aligned}
{}^4_8\boldsymbol{T}'_{\text{lap}} &= \begin{bmatrix} Rot(y_4, \alpha + 90^\circ) & \begin{matrix}0\\0\\0\end{matrix} \\ 0\ 0\ 0 & 1 \end{bmatrix}^{-1} \cdot {}^4_5\boldsymbol{T}_{\text{lap}} \cdot {}^5_6\boldsymbol{T}_{\text{lap}} \cdot {}^6_7\boldsymbol{T}_{\text{lap}} \cdot {}^7_8\boldsymbol{T}_{\text{lap}}\\
&= \begin{bmatrix} s_5 & -c_5s_{6-\beta-\gamma} & -c_5c_{6-\beta-\gamma} & (d_{\text{j}} + d_7)c_5c_{6-\beta} \\ -c_5 & -s_5s_{6-\beta-\gamma} & -s_5c_{6-\beta-\gamma} & (d_{\text{j}} + d_7)s_5c_{6-\beta} \\ 0 & c_{6-\beta-\gamma} & -s_{6-\beta-\gamma} & d_6 + (d_{\text{j}} + d_7)s_{6-\beta} \\ 0 & 0 & 0 & 1 \end{bmatrix}.
\end{aligned} \tag{4}
$$

Therefore, the coordinate transformation ${}^0_{4\text{new}}\boldsymbol{T}$ from the frame ${}_{\text{lap}}O_0$ to ${}_{\text{lap}}O'_4$ is given by Eq. (5), and is a constant matrix and easy to get ${}^0_{4\text{new}}\boldsymbol{T}^{-1}$:

$$
{}^0_{4\text{new}}\boldsymbol{T} = {}^0_4\boldsymbol{T}_{\text{pas}} \cdot \begin{bmatrix} Rot(y_4, \alpha + 90^\circ) & 0 \\ 0 & 1 \end{bmatrix}. \tag{5}
$$

Suppose that matrix ${}^0_8\boldsymbol{T}^{\text{lap}}_{\text{target}}$ is the desired PAO of the TCS ${}_{\text{lap}}O_8$ with respect to the frame ${}_{\text{lap}}O_0$, the PAO with respect to the frame ${}_{\text{lap}}O'_4$ can be calculated by Eq. (6):

$$
{}^4_8\boldsymbol{T}'_{\text{lap}} = {}^0_{4\text{new}}\boldsymbol{T}^{-1} \cdot {}^0_8\boldsymbol{T}_{\text{target}} = \begin{bmatrix} {}^{\text{tar}}_{\text{lap}}n_x & {}^{\text{tar}}_{\text{lap}}o_x & {}^{\text{tar}}_{\text{lap}}a_x & {}^{\text{tar}}_{\text{lap}}p_x \\ {}^{\text{tar}}_{\text{lap}}n_y & {}^{\text{tar}}_{\text{lap}}o_y & {}^{\text{tar}}_{\text{lap}}a_y & {}^{\text{tar}}_{\text{lap}}p_y \\ {}^{\text{tar}}_{\text{lap}}n_z & {}^{\text{tar}}_{\text{lap}}o_z & {}^{\text{tar}}_{\text{lap}}a_z & {}^{\text{tar}}_{\text{lap}}p_z \\ 0 & 0 & 0 & 1 \end{bmatrix}. \tag{6}
$$

According to Eq. (6), the desired position vector is shown as $\boldsymbol{T}^{\text{lap}}_{\text{target}} = \left[{}^{\text{tar}}_{\text{lap}}p_x\ {}^{\text{tar}}_{\text{lap}}p_y\ {}^{\text{tar}}_{\text{lap}}p_z\right]^{\text{T}}$. Simultaneously using Eqs. (4) and (6), the only solutions of the inverse kinematics are calculated as follows:

$$
\begin{aligned}
\text{The joint range of motion}: &\begin{cases} \theta_5 \in (-90^\circ, 90^\circ) \\ \theta_6 \in (\beta - 90^\circ, \beta + 90^\circ), \\ d_7 \in (-150, 120)\ \text{mm} \end{cases}\\
\theta_5 &= \arctan\left({}^{\text{tar}}_{\text{lap}}p_y \big/ {}^{\text{tar}}_{\text{lap}}p_x\right),\\
\text{If angle}\,\theta_5 \neq 0,\ \theta_6 &= \arctan 2\left[\left({}^{\text{tar}}_{\text{lap}}p_z - d_6\right), {}^{\text{tar}}_{\text{lap}}p_y \big/ \sin(\theta_5)\right] + \beta,\\
\text{If angle}\,\theta_5 = 0, \theta_6 &= \arctan 2\left[\left({}^{\text{tar}}_{\text{lap}}p_z - d_6\right), {}^{\text{tar}}_{\text{lap}}p_x\right] + \beta,\\
d_7 &= {}^{\text{tar}}_{\text{lap}}p_x / \left[\cos(\theta_5) \cdot \cos(\theta_6 - \beta)\right] - d_{\text{j}}.
\end{aligned}
$$

https://doi.org/10.1017/S026357471300088X Published online by Cambridge University Press

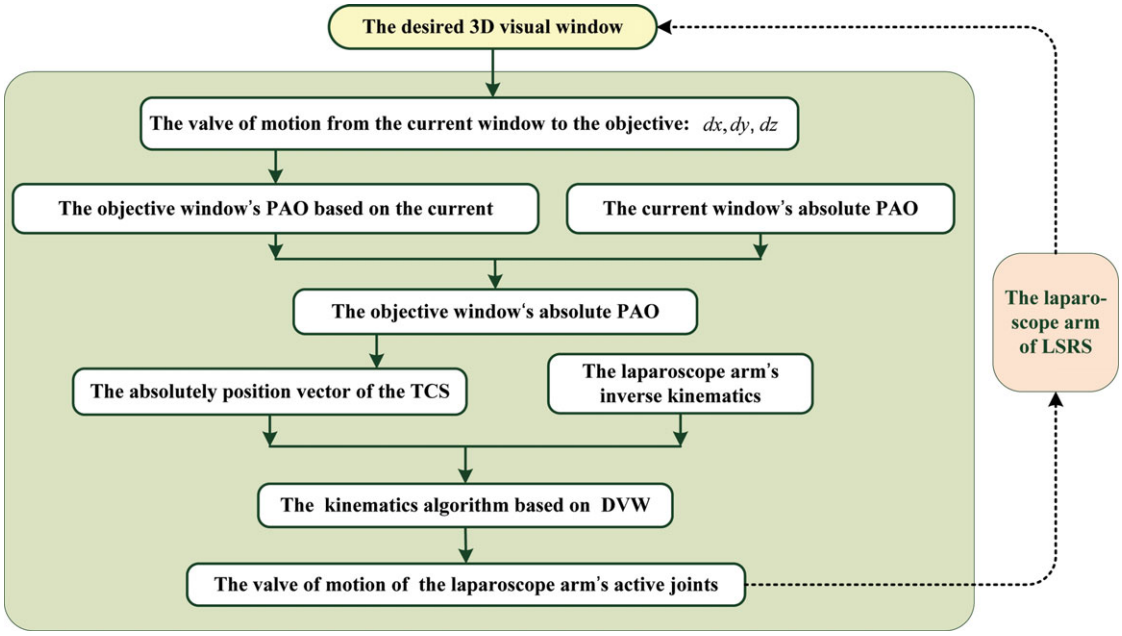


Fig. 5. (Colour online) The technological flow diagram of the laparoscope arm's kinematics algorithm based on DVW.

4.2. Kinematics algorithm based on the DVW of the laparoscope arm

According to Section 2.1, the kinematics algorithm is established through an analysis of the relations between the objective visual window and the current based on the kinematical model; the technological flow diagram is shown in Fig. 5.

According to Eq. (3), the absolute position vector of the current visual window with respect to the normalized BCS is given by the position vector $\left[{}_{\text{lap}}p_x \ {}_{\text{lap}}p_y \ {}_{\text{lap}}p_z\right]^{\text{T}}$. And (dx, dy, dz) are the values of motion along the three axes of laparoscope's TCS for obtaining the objective window's position with respect to the TCS ${}_{\text{lap}}O_8$ of the current window; the objective window's position vector is given by Eq. (7):

$$ {}^{\text{vis}}_{\text{lap}}\boldsymbol{T} = \left[{}^{\text{vis}}_{\text{lap}}p_x \, {}^{\text{vis}}_{\text{lap}}p_y \, {}^{\text{vis}}_{\text{lap}}p_z\right]^{\text{T}}, \tag{7} $$

where

$$ \begin{aligned} {}^{\text{vis}}_{\text{lap}}p_x &= {}_{\text{lap}}p_x + {}_{\text{lap}}n_x \cdot dx + {}_{\text{lap}}o_x \cdot dy + {}_{\text{lap}}a_x \cdot dz, \\ {}^{\text{vis}}_{\text{lap}}p_y &= {}_{\text{lap}}p_y + {}_{\text{lap}}n_y \cdot dx + {}_{\text{lap}}o_y \cdot dy + {}_{\text{lap}}a_y \cdot dz, \\ {}^{\text{vis}}_{\text{lap}}p_z &= {}_{\text{lap}}p_z + {}_{\text{lap}}n_z \cdot dx + {}_{\text{lap}}o_z \cdot dy + {}_{\text{lap}}a_z \cdot dz. \end{aligned} $$

According to Eq. (6), the absolute position vector of the objective window based on the normalized BCS is given by Eq. (8):

$$ \begin{bmatrix} {}^{\text{vis}}_{\text{tar}}\boldsymbol{T} \\ 1 \end{bmatrix} = {}^{0}_{4\text{new}}\boldsymbol{T}^{-1} \cdot \begin{bmatrix} {}^{\text{vis}}_{\text{lap}}\boldsymbol{T} \\ 1 \end{bmatrix} = \left[{}^{\text{vis}}_{\text{tar}}p_x \, {}^{\text{vis}}_{\text{tar}}p_y \, {}^{\text{vis}}_{\text{tar}}p_z \, 1\right]^{\text{T}}. \tag{8} $$

https://doi.org/10.1017/S026357471300088X Published online by Cambridge University Press

Substituting matrix ${}^{\text{vis}}_{\text{tar}}\boldsymbol{T}$ to the solutions of inverse kinematics, the equations of the laparoscope arm's kinematics algorithm based on the DVW are given below:

$$\text{The joint range of motion}: \begin{cases} \theta_5 \in (-90^\circ, 90^\circ) \\ \theta_6 \in (\beta - 90^\circ, \beta + 90^\circ), \\ d_7 \in (-150, 120)\ \text{mm} \end{cases}$$

$$\theta_5 = \arctan({}^{\text{vis}}_{\text{tar}}p_y / {}^{\text{vis}}_{\text{tar}}p_x),$$

$$\text{If angle}\,\theta_5 \neq 0, \theta_6 = \arctan 2\left[({}^{\text{vis}}_{\text{tar}}p_z - d_6), {}^{\text{vis}}_{\text{tar}}p_y / \sin(\theta_5)\right] + \beta,$$

$$\text{If angle}\,\theta_5 = 0, \theta_6 = \arctan 2\left[({}^{\text{vis}}_{\text{tar}}p_z - d_6), {}^{\text{vis}}_{\text{tar}}p_x\right] + \beta,$$

$$d_7 = {}^{\text{vis}}_{\text{tar}}p_x / \left[\cos(\theta_5) \cdot \cos(\theta_6 - \beta)\right] - d_{\text{j}}.$$

Because of the practical function of the laparoscope arm and only three active joints being driven by the servo motors, we decide to control the position for the kinematics algorithm based on the DVW, and the laparoscope's PAO is calculated with the laparoscope's position and the orientation of the trocar's point of tangency that we already know.

5. The Kinematics Algorithm Based on DVW for the Instrument Arm

It is significant to control the instruments based on the 3D visual window with the visual feedback, so that devices' motion of the instrument arms in the 3D visual window and the master–slave manipulation of the LSRS can be consistent; it is suitable for doctors' visual and operation habits. Therefore, we analyse the kinematics model and establish its kinematics algorithm based on the DVW as in Section 4.

5.1. Kinematical modelling of the instrument arm

According to the same structural features of the two instrument arms, their coordinate systems are the same except for their BCSs; the kinematics coordinate systems are established as shown in Fig. 6. The frame ${}_{\text{dev}}O_0$ is its own BCS, the frames ${}_{\text{dev}}O_1, {}_{\text{dev}}O_2, {}_{\text{dev}}O_3, {}_{\text{dev}}O_4$ are the first four passive joints' coordinate systems, the frame ${}_{\text{dev}}O_{11}$ is the TCS, and the other coordinate systems are the active joints driven by the servo motors. According to the LSRS structure, the analysis method is similar to Section 4.

According to above, matrix ${}^{4}_{11}\boldsymbol{T}_{\text{act}}$ is the coordinate transformation from the TCS ${}_{\text{dev}}O_{11}$ to the fourth frame ${}_{\text{dev}}O_4$ as shown below:

$${}^{4}_{11}\boldsymbol{T}_{\text{act}} = {}^{4}_{5}\boldsymbol{T}_{\text{act}} \cdot {}^{5}_{6}\boldsymbol{T}_{\text{act}} \cdot {}^{6}_{7}\boldsymbol{T}_{\text{act}} \cdot {}^{7}_{8}\boldsymbol{T}_{\text{act}} \cdot {}^{8}_{9}\boldsymbol{T}_{\text{act}} \cdot {}^{9}_{10}\boldsymbol{T}_{\text{act}} \cdot {}^{10}_{11}\boldsymbol{T}_{\text{act}}. \tag{9}$$

Simultaneously using Eqs. (1), (2) and (9), the coordinate transformation of the forward kinematics from the normalized BCS ${}_{\text{lap}}O_0$ to the TCS ${}_{\text{dev}}O_{11}$ is given by Eq. (10):

$${}^{\text{B}}_{11}\boldsymbol{T}_{\text{dev}} = {}^{\text{B}}_{\text{dev}}\boldsymbol{T}_{\lambda} \cdot {}^{0}_{4}\boldsymbol{T}_{\text{pas}} \cdot {}^{4}_{11}\boldsymbol{T}_{\text{act}} = \begin{bmatrix} {}_{\text{dev}}n_x & {}_{\text{dev}}o_x & {}_{\text{dev}}a_x & {}_{\text{dev}}p_x \\ {}_{\text{dev}}n_y & {}_{\text{dev}}o_y & {}_{\text{dev}}a_y & {}_{\text{dev}}p_y \\ {}_{\text{dev}}n_z & {}_{\text{dev}}o_z & {}_{\text{dev}}a_z & {}_{\text{dev}}p_z \\ 0 & 0 & 0 & 1 \end{bmatrix}, \tag{10}$$

where

$${}_{\text{dev}}n_x = c_{2+3+4}(s_{10}(c_{\beta-6}s_7c_\alpha - s_{\beta-6}c_5s_7s_\alpha + c_7s_5s_\alpha)\cdots,$$

$${}_{\text{dev}}p_z = d_1 + d_4 + (d_8 + d_9 + d_{10}c_9 + d_{11}c_{10}c_9)\cdots.$$

There are six active joints driven by the servo motors, so their inverse kinematics is calculated based on the fourth passive coordinate system ${}_{\text{dev}}O_4$. In order to simplify the calculation, we try

https://doi.org/10.1017/S026357471300088X Published online by Cambridge University Press

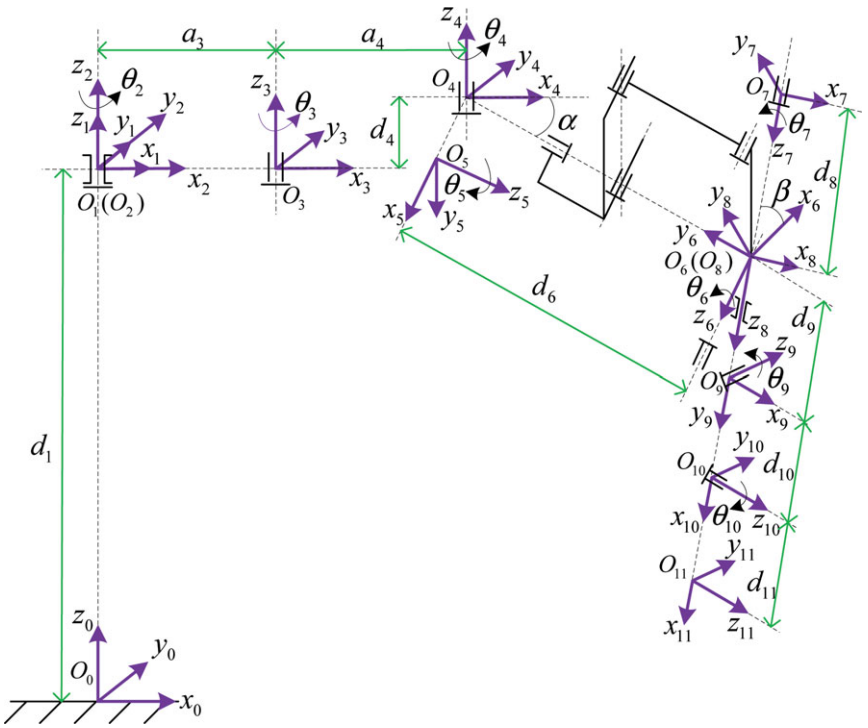


Fig. 6. (Colour online) The kinematics coordinate systems of the instrument arm.

to roll the frame ${}_{\text{dev}}O_4$ along its axis y_4 for $(\alpha + 90^\circ)$ as a new frame ${}_{\text{dev}}O'_4$, and the coordinate transformation ${}^{4}_{11}\boldsymbol{T}'_{\text{act}}$ from the frame ${}_{\text{dev}}O'_4$ to ${}_{\text{dev}}O_{11}$ is given by Eq. (11):

$$ {}^{4}_{11}\boldsymbol{T}'_{\text{act}} = \begin{bmatrix} Rot(y_4, \alpha + 90^\circ) & 0 \\ 0 & 1 \end{bmatrix}^{-1} \cdot {}^{4}_{5}\boldsymbol{T}_{\text{act}} \cdot {}^{5}_{6}\boldsymbol{T}_{\text{act}} \cdot {}^{6}_{7}\boldsymbol{T}_{\text{act}} \cdot {}^{7}_{8}\boldsymbol{T}_{\text{act}} \cdot {}^{8}_{9}\boldsymbol{T}_{\text{act}} \cdot {}^{9}_{10}\boldsymbol{T}_{\text{act}} \cdot {}^{10}_{11}\boldsymbol{T}_{\text{act}}. \tag{11} $$

Simultaneously using Eqs. (1) and (2), the coordinate transformation ${}^{\text{B}}_{4\text{new}}\boldsymbol{T}_{\text{dev}}$ from the normalized BCS ${}_{\text{lap}}O_0$ to the frame ${}_{\text{dev}}O'_4$ is given by Eq. (12), and it is a constant matrix and its inverse matrix ${}^{0}_{4\text{new}}\boldsymbol{T}^{-1}$ is easy to get:

$$ {}^{\text{B}}_{4\text{new}}\boldsymbol{T}_{\text{dev}} = {}^{\text{B}}_{\text{dev}}\boldsymbol{T}_{\lambda} \cdot {}^{0}_{4}\boldsymbol{T}_{\text{pas}} \cdot \begin{bmatrix} Rot(y_4, \alpha + 90^\circ) & 0 \\ 0 & 1 \end{bmatrix}. \tag{12} $$

Supposing matrix ${}^{\text{B}}_{\text{target}}\boldsymbol{T}_{\text{dev}}$ is the desired PAO of the TCS ${}_{\text{dev}}O_{11}$ with respect to ${}_{\text{lap}}O_0$, the PAO with respect to the coordinate system ${}_{\text{dev}}O'_4$ can be calculated as follows:

$$ {}^{4}_{11}\boldsymbol{T}'_{\text{act}} = {}^{\text{B}}_{4}\boldsymbol{T}^{-1}_{\text{dev}} \cdot {}^{\text{B}}_{\text{target}}\boldsymbol{T}_{\text{dev}}. \tag{13} $$

Supposing its inverse matrix is $({}^{4}_{11}\boldsymbol{T}'_{\text{act}})^{-1}$, as shown below:

$$ ({}^{4}_{11}\boldsymbol{T}'_{\text{act}})^{-1} = \begin{bmatrix} {}_{\text{d}}n'_x & {}_{\text{d}}o'_x & {}_{\text{d}}a'_x & {}_{\text{d}}p'_x \\ {}_{\text{d}}n'_y & {}_{\text{d}}o'_y & {}_{\text{d}}a'_y & {}_{\text{d}}p'_y \\ {}_{\text{d}}n'_z & {}_{\text{d}}o'_z & {}_{\text{d}}a'_z & {}_{\text{d}}p'_z \\ 0 & 0 & 0 & 1 \end{bmatrix}. \tag{14} $$

(i) Let us transform Eq. (11) as Eq. (15), for solving $\theta_{10}, \theta_9, d_8$:

$$ ({}^{4}_{11}\boldsymbol{T}'_{\text{act}})^{-1} \cdot {}^{4}_{5}\boldsymbol{T}_{\text{act}} \cdot {}^{5}_{6}\boldsymbol{T}_{\text{act}} \cdot {}^{6}_{7}\boldsymbol{T}_{\text{act}} = {}^{10}_{11}\boldsymbol{T}^{-1}_{\text{act}} \cdot {}^{9}_{10}\boldsymbol{T}^{-1}_{\text{act}} \cdot {}^{8}_{9}\boldsymbol{T}^{-1}_{\text{act}} \cdot {}^{7}_{8}\boldsymbol{T}^{-1}_{\text{act}}. \tag{15} $$

https://doi.org/10.1017/S026357471300088X Published online by Cambridge University Press

(ii) Let us transform Eq. (11) as Eq. (16), for solving $\theta_7, \theta_6, \theta_5$:

$$ {}^{4}_{5}\boldsymbol{T}'_{\text{act}} \cdot {}^{5}_{6}\boldsymbol{T}_{\text{act}} \cdot {}^{6}_{7}\boldsymbol{T}_{\text{act}} = {}^{4}_{11}\boldsymbol{T}'_{\text{act}} \cdot {}^{10}_{11}\boldsymbol{T}^{-1}_{\text{act}} \cdot {}^{9}_{10}\boldsymbol{T}^{-1}_{\text{act}} \cdot {}^{8}_{9}\boldsymbol{T}^{-1}_{\text{act}} \cdot {}^{7}_{8}\boldsymbol{T}^{-1}_{\text{act}}. \tag{16} $$

Simultaneously using Eqs. (15), (16) and the correlation parameters, and supposing the right-hand side of Eq. (16) is matrix ${}^{(14)}_{\text{right}}\boldsymbol{T}_{\text{dev}}$, we have

$$ {}^{(14)}_{\text{right}}\boldsymbol{T}_{\text{dev}} = \begin{bmatrix} T_{11} & T_{12} & T_{13} & T_{14} \\ T_{21} & T_{22} & T_{23} & T_{24} \\ T_{31} & T_{32} & T_{33} & T_{34} \\ T_{41} & T_{42} & T_{43} & T_{44} \end{bmatrix}. \tag{17} $$

Simultaneously using above correlation equations, we can calculate the only solutions of inverse kinematics as follows:

$$ \text{The joint range of motion}: \begin{cases} \theta_{10} \in (-90^\circ, 90^\circ) \\ \theta_9 \in (-90^\circ, 90^\circ) \\ d_8 \in (-200, 150)\ \text{mm} \end{cases}, \begin{cases} \theta_7 \in (-180^\circ, 180^\circ) \\ \theta_6 \in (\beta - 90^\circ, \beta + 90^\circ), \\ \theta_5 \in (-90^\circ, 90^\circ) \end{cases} $$

$$ \theta_{10} = \arctan\left[({}_{\text{d}}p'_y + {}_{\text{d}}a'_y \cdot d_6)/({}_{\text{d}}p'_x + {}_{\text{d}}a'_x \cdot d_6 + d_{11})\right], $$

$$ \text{If angle } \theta_{10} \neq 0, \theta_9 = \arctan\left\{({}_{\text{d}}p'_z + {}_{\text{d}}a'_z \cdot d_6)/\left[d_{10} - ({}_{\text{d}}p'_y + {}_{\text{d}}a'_y \cdot d_6)/\sin(\theta_{10})\right]\right\}, $$

$$ \text{If angle } \theta_{10} = 0, \theta_9 = \arctan\left[({}_{\text{d}}p'_z + {}_{\text{d}}a'_z \cdot d_6)/({}_{\text{d}}p'_x + {}_{\text{d}}a'_x \cdot d_6 + \text{d}_{11} + d_{10})\right], $$

$$ d_8 = -\left[{}_{\text{d}}p'_x + {}_{\text{d}}a'_z \cdot d_6 + d_{11} + d_{10} \cdot \cos(\theta_{10}) + d_9 \cdot \cos(\theta_9)\right] / \left[\cos(\theta_{10}) \cdot \cos(\theta_9)\right], $$

$$ \theta_7 = \arctan 2\left[T_{32}/\cos(\theta_6 - \beta), -T_{31}/\cos(\theta_6 - \beta)\right], $$

$$ \theta_6 = \beta + \arctan\left[T_{33} \cdot \cos(\theta_5)/T_{13}\right], $$

$$ \theta_5 = \arctan(T_{23}/T_{13}). $$

5.2. Kinematics algorithm based on the DVW of the instrument arm

In Section 2.2, the kinematics algorithm is established through an analysis of the relations between the visual window and the instrument based on the kinematical model; the technological flow diagram is shown in Fig. 7.

According to the kinematics of the instrument and laparoscope arms, the PAO of the instrument's TCS with respect to the laparoscope's TCS is calculated, and the coordinate transformation matrix ${}^{\text{dev}}\boldsymbol{T}_{\text{lap}}$ is given by

$$ \boldsymbol{T}_{\text{lap}} \cdot {}^{\text{dev}}\boldsymbol{T}_{\text{lap}} = \boldsymbol{T}_{\text{dev}}, \tag{18} $$

where matrix $\boldsymbol{T}_{\text{lap}}$ represents the laparoscope's PAO based on the normalized BCS, and matrix $\boldsymbol{T}_{\text{dev}}$ represents the instrument arm's PAO based on the normalized BCS.

To simplify the analysis, we use $(\psi, \phi, \varphi, {}_{\text{vis}}p_x, {}_{\text{vis}}p_y, {}_{\text{vis}}p_z)$ to describe matrix${}^{\text{dev}}\boldsymbol{T}_{\text{lap}}$, and (ψ, ϕ, φ) are the RPY angles for describing the orientation matrix, and $[{}_{\text{vis}}p_x, {}_{\text{vis}}p_y, {}_{\text{vis}}p_z]^{\text{T}}$ is the position vector.

Suppose $(d\psi, d\phi, d\varphi, dx, dy, dz)$ are the values of desired instrument's motion with respect to the current that is according to the doctor's demands.

Therefore,$(\psi', \phi', \varphi', {}_{\text{vis}}p'_x, {}_{\text{vis}}p'_y, {}_{\text{vis}}p'_z)$ are the objective parameters of the instrument arm with respect to the $\text{TCS}_{\text{lap}}O_8$, as shown below:

$$ \begin{cases} \psi' = \psi + d\psi \\ \phi' = \phi + d\phi \\ \varphi' = \varphi + d\varphi \end{cases}, \tag{19} $$

https://doi.org/10.1017/S026357471300088X Published online by Cambridge University Press

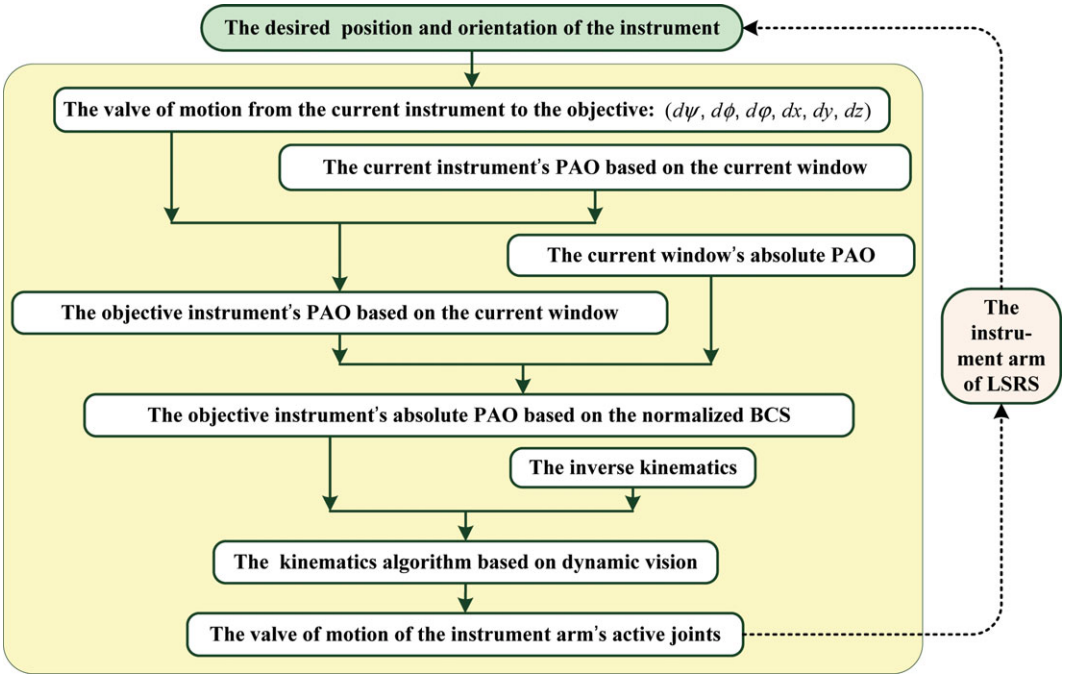


Fig. 7. (Colour online) The technological flow diagram of the instrument arm's kinematics algorithm based on DVW.

$$\begin{bmatrix} {}^{\text{lap}}p'_x \\ {}^{\text{lap}}p'_y \\ {}^{\text{lap}}p'_z \end{bmatrix} = \begin{bmatrix} {}^{\text{lap}}p_x \\ {}^{\text{lap}}p_y \\ {}^{\text{lap}}p_z \end{bmatrix} + \boldsymbol{R}_{\text{tar}} \cdot \begin{bmatrix} dx \\ dy \\ dz \end{bmatrix}, \tag{20}$$

where

$$\boldsymbol{R}_{\text{tar}} = \begin{bmatrix} c\psi' c\phi' & c\psi' s\phi' s\varphi' - c\varphi' s\psi' & s\psi' s\varphi' + c\psi' c\varphi' s\phi' \\ c\phi' s\psi' & c\psi' c\varphi' + s\psi' s\phi' s\varphi' & c\varphi' s\psi' s\phi' - c\psi' s\varphi' \\ -s\phi' & c\phi' s\varphi' & c\phi' c\varphi' \end{bmatrix}. \tag{21}$$

Simultaneously using Eqs. (19)–(21), the instrument arm's objective PAO based on the visual window is given by

$${}^{\text{dev}}\boldsymbol{T}'_{\text{lap}} = \begin{bmatrix} & & & {}^{\text{lap}}p'_x \\ & \boldsymbol{R}_{\text{tar}} & & {}^{\text{lap}}p'_y \\ & & & {}^{\text{lap}}p'_z \\ 0 & 0 & 0 & 1 \end{bmatrix}. \tag{22}$$

According to Eq. (18), matrix $\boldsymbol{T}^{\text{B}}_{\text{dev}}$ is given by $\boldsymbol{T}^{\text{B}}_{\text{dev}} = \boldsymbol{T}_{\text{lap}} \cdot {}^{\text{dev}}\boldsymbol{T}'_{\text{lap}}$, which is the objective instrument arm's absolute PAO based on the normalized BCS.

Simultaneously using above correlation equations, matrix $\boldsymbol{T}^{\text{B}}_{\text{dev}}$ is shown in Eq. (23) and its inverse matrix $\boldsymbol{T}^{\text{B}-1}_{\text{dev}}$ is shown in Eq. (24):

$$\boldsymbol{T}^{\text{B}}_{\text{dev}} = \begin{bmatrix} {}^{\text{vis}}_{\text{dev}}n_x & {}^{\text{vis}}_{\text{dev}}o_x & {}^{\text{vis}}_{\text{dev}}a_x & {}^{\text{vis}}_{\text{dev}}p_x \\ {}^{\text{vis}}_{\text{dev}}n_y & {}^{\text{vis}}_{\text{dev}}o_y & {}^{\text{vis}}_{\text{dev}}a_y & {}^{\text{vis}}_{\text{dev}}p_y \\ {}^{\text{vis}}_{\text{dev}}n_z & {}^{vis}_{dev}o_z & {}^{\text{vis}}_{\text{dev}}a_z & {}^{\text{vis}}_{\text{dev}}p_z \\ 0 & 0 & 0 & 1 \end{bmatrix}, \tag{23}$$

https://doi.org/10.1017/S026357471300088X Published online by Cambridge University Press

$$\boldsymbol{T}_{\text{dev}}^{\text{B}-1} = \begin{bmatrix} {}^{\text{vis}}_{\text{dev}}n'_x & {}^{\text{vis}}_{\text{dev}}o'_x & {}^{\text{vis}}_{\text{dev}}a'_x & {}^{\text{vis}}_{\text{dev}}p'_x \\ {}^{\text{vis}}_{\text{dev}}n'_y & {}^{\text{vis}}_{\text{dev}}o'_y & {}^{\text{vis}}_{\text{dev}}a'_y & {}^{\text{vis}}_{\text{dev}}p'_y \\ {}^{\text{vis}}_{\text{dev}}n'_z & {}^{\text{vis}}_{\text{dev}}o'_z & {}^{\text{vis}}_{\text{dev}}a'_z & {}^{\text{vis}}_{\text{dev}}p'_z \\ 0 & 0 & 0 & 1 \end{bmatrix}. \tag{24}$$

According to the instrument arm's inverse kinematics, by substituting matrix $\boldsymbol{T}_{\text{dev}}^{\text{B}}$ as ${}^{\text{B}}_{\text{target}}\boldsymbol{T}_{\text{dev}}$ into Eq. (13), matrix ${}^{4}_{11}\boldsymbol{T}_{\text{act}}^{\text{B}}$ is given by Eq. (25) and its inverse matrix ${}^{4}_{11}\boldsymbol{T}_{\text{act}}^{\text{B}-1}$ is shown in Eq. (26):

$${}^{4}_{11}\boldsymbol{T}_{\text{act}}^{\text{B}} = {}^{\text{B}}_{4\text{new}}\boldsymbol{T}_{\text{dev}}^{-1} \cdot \boldsymbol{T}_{\text{dev}}^{\text{B}} = \begin{bmatrix} {}^{\text{B}}_{\text{d}}n_x & {}^{\text{B}}_{\text{d}}o_x & {}^{\text{B}}_{\text{d}}a_x & {}^{\text{B}}_{\text{d}}p_x \\ {}^{\text{B}}_{\text{d}}n_y & {}^{\text{B}}_{\text{d}}o_y & {}^{\text{B}}_{\text{d}}a_y & {}^{\text{B}}_{\text{d}}p_y \\ {}^{\text{B}}_{\text{d}}n_z & {}^{\text{B}}_{\text{d}}o_z & {}^{\text{B}}_{\text{d}}a_z & {}^{\text{B}}_{\text{d}}p_z \\ 0 & 0 & 0 & 1 \end{bmatrix}, \tag{25}$$

$${}^{4}_{11}\boldsymbol{T}_{\text{act}}^{\text{B}-1} = \begin{bmatrix} {}^{\text{B}}_{\text{d}}n'_x & {}^{\text{B}}_{\text{d}}o'_x & {}^{\text{B}}_{\text{d}}a'_x & {}^{\text{B}}_{\text{d}}p'_x \\ {}^{\text{B}}_{\text{d}}n'_y & {}^{\text{B}}_{\text{d}}o'_y & {}^{\text{B}}_{\text{d}}a'_y & {}^{\text{B}}_{\text{d}}p'_y \\ {}^{\text{B}}_{\text{d}}n'_z & {}^{\text{B}}_{\text{d}}o'_z & {}^{\text{B}}_{\text{d}}a'_z & {}^{\text{B}}_{\text{d}}p'_z \\ 0 & 0 & 0 & 1 \end{bmatrix}. \tag{26}$$

Substituting matrix ${}^{4}_{11}\boldsymbol{T}_{\text{act}}^{\text{B}}$ instead of ${}^{4}_{11}\boldsymbol{T}_{\text{act}}$ to Eq. (16) and supposing matrix ${}^{(14)}_{\text{right}}\boldsymbol{T}_{\text{dev}}^{\text{vis}}$ as the right end of Eq. (16), we have

$${}^{(14)}_{\text{right}}\boldsymbol{T}_{\text{dev}}^{\text{vis}} = \begin{bmatrix} {}^{\text{vis}}T_{11} & {}^{\text{vis}}T_{12} & {}^{\text{vis}}T_{13} & {}^{\text{vis}}T_{14} \\ {}^{\text{vis}}T_{21} & {}^{\text{vis}}T_{22} & {}^{\text{vis}}T_{23} & {}^{\text{vis}}T_{24} \\ {}^{\text{vis}}T_{31} & {}^{\text{vis}}T_{32} & {}^{\text{vis}}T_{33} & {}^{\text{vis}}T_{34} \\ {}^{\text{vis}}T_{41} & {}^{\text{vis}}T_{42} & {}^{\text{vis}}T_{43} & {}^{\text{vis}}T_{44} \end{bmatrix}. \tag{27}$$

Substituting Eqs. (26) and (27) to the solutions of inverse kinematics of the instrument arm in Section 5.1, the equations of kinematics algorithm based on the DVW of the instrument arm are given below:

$$\text{The joint range of motion}: \begin{cases} \theta_{10} \in (-90^\circ, 90^\circ) \\ \theta_9 \in (-90^\circ, 90^\circ) \\ d_8 \in (-200, 150)\ \text{mm} \end{cases}, \begin{cases} \theta_7 \in (-180^\circ, 180^\circ) \\ \theta_6 \in (\beta - 90^\circ, \beta + 90^\circ), \\ \theta_5 \in (-90^\circ, 90^\circ) \end{cases}$$

$$\theta_{10} = \arctan\left[({}^{\text{B}}_{\text{d}}p'_y + {}^{\text{B}}_{\text{d}}a'_y \cdot d_6)/({}_{\text{d}}p'_x + {}_{\text{d}}a'_x \cdot d_6 + d_{11})\right],$$

$$\text{If angle } \theta_{10} \neq 0, \theta_9 = \arctan\left\{({}^{\text{B}}_{\text{d}}p'_z + {}^{\text{B}}_{\text{d}}a'_z \cdot d_6)/\left[d_{10} - ({}^{\text{B}}_{\text{d}}p'_y + {}^{\text{B}}_{\text{d}}a'_y \cdot d_6)/\sin(\theta_{10})\right]\right\},$$

$$\text{If angle } \theta_{10} = 0, \theta_9 = \arctan\left[({}^{\text{B}}_{\text{d}}p'_z + {}^{\text{B}}_{\text{d}}a'_z \cdot d_6)/({}^{\text{B}}_{\text{d}}p'_x + {}^{\text{B}}_{\text{d}}a'_x \cdot d_6 + \text{d}_{11} + d_{10})\right],$$

$$d_8 = -\left[{}^{\text{B}}_{\text{d}}p'_x + {}^{\text{B}}_{\text{d}}a'_z \cdot d_6 + d_{11} + d_{10} \cdot \cos(\theta_{10}) + d_9 \cdot \cos(\theta_9)\right] / \left[\cos(\theta_{10}) \cdot \cos(\theta_9)\right],$$

$$\theta_7 = \arctan 2\left[{}^{\text{vis}}T_{32}/\cos(\theta_6 - \beta), -{}^{\text{vis}}T_{31}/\cos(\theta_6 - \beta)\right],$$

$$\theta_6 = \beta + \arctan\left[{}^{\text{vis}}T_{33} \cdot \cos(\theta_5)/{}^{\text{vis}}T_{13}\right],$$

$$\theta_5 = \arctan({}^{\text{vis}}T_{23}/{}^{\text{vis}}T_{13}).$$

6. Hybrid Simulation Analysis Based on MATLAB

We have developed the simulation experiments based on the Simulink and SimMechanics toolboxes, in order to verify the correctness and feasibility of kinematics algorithms mentioned above. The forward and inverse kinematics are verified, and the hybrid simulation models for kinematics algorithms are set up.

6.1. Simulation of the kinematics algorithm based on the DVW for the laparoscope arm

6.1.1. Kinematics simulation of the laparoscope arm. A group of constants is supposed to be the link parameters as show in Table I, for inputting to the laparoscope arm's kinematics. The model of the simulation based on Simulink is set up as shown in Fig. 8. And three random digits created by

https://doi.org/10.1017/S026357471300088X Published online by Cambridge University Press

Table I. The link parameters of the laparoscope arm.

θ_2	θ_3	θ_4	α	β	d_1	a_3	a_4	d_4	d_6	d_j
45°	45°	45°	45°	30°	1800 mm	400 mm	450 mm	180 mm	700 mm	150 mm

Table II. The input and output parameters of the laparoscope arm's simulation analysis.

No.	θ_5 (rad)	θ_6 (rad)	d_7 (mm)
1	−1.4630	0.3312	95.02
2	0.4158	−0.7408	91.34
3	0.6577	1.3240	64.63

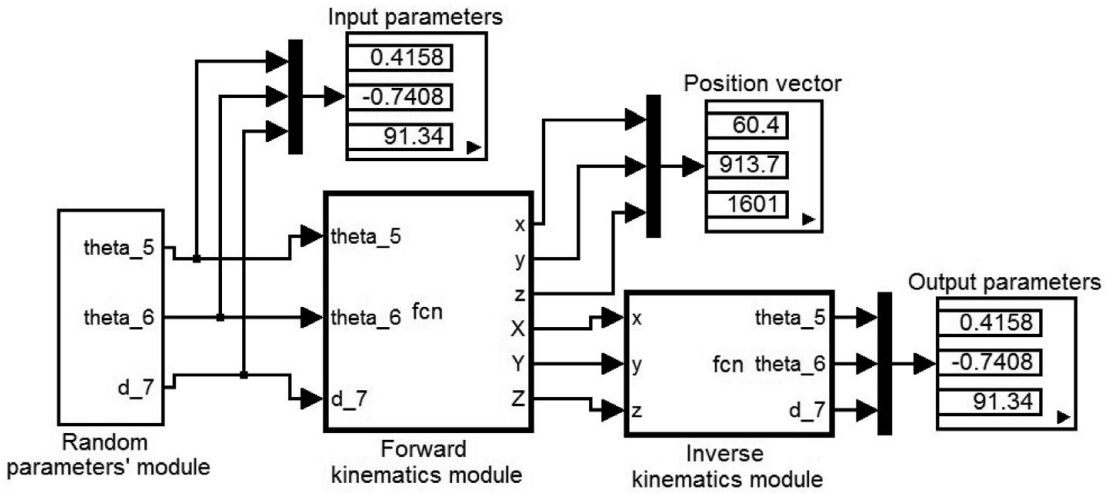


Fig. 8. The Simulink simulation of the laparoscope arm's kinematics model.

the computer are chosen in the parameter scope of the active joints, they are input to the forward kinematics, the result of the position vector is input to the inverse kinematics, and the outputs are θ_5, θ_6, d_7. Therefore, the kinematics is corrected through a comparison of the input and output parameters and the numerical examples are shown in Table II.

6.1.2. Hybrid simulation of the laparoscope arm's kinematics algorithm based on the DVW. The hybrid simulation model is set up by the Simulink and SimMechanics toolboxes according to the laparoscope arm's kinematics algorithm based on the DVW in Section 4.2, as shown in Fig. 9, and the subsystem of the current and objective mechanisms is shown in Fig. 10. The desired output is calculated by the Simulink model and the practical output comes from the SimMechanics model; the two outputs equally represent the correctness of the laparoscope arm's kinematics algorithm based on the DVW.

We simultaneously use the parameters in Tables I–III as inputs to the hybrid simulation model and three groups of outputs are shown in Table IV. The desired D-value (${}^{abs}\Delta px$, ${}^{abs}\Delta py$, ${}^{abs}\Delta pz$) of motion of the objective visual window based on the current is calculated from the Simulink model, and the practical D-value (${}^{rel}\Delta px$,${}^{rel}\Delta py$,${}^{rel}\Delta pz$) of motion is calculated from the SimMechanics model. The two D-value outputs are the evidence to prove the correctness of the laparoscope arm's kinematics algorithm proposed in this study.

6.2. Simulation of the kinematics algorithm based on the DVW for the instrument arm

The instrument arms of the LSRS consist of two symmetrically set identical arms 1 and 2, except for the mounting position. Therefore, the simulation processes are the same, and the instrument arm 1 is chosen for the simulation analysis.

https://doi.org/10.1017/S026357471300088X Published online by Cambridge University Press

Table III. The value of motion of the objective window with respect to the current.

No.	dx (mm)	dy (mm)	dz (mm)
1	−20.23	30.56	70.85
2	−41.22	88.28	95.12
3	27.35	−56.87	13.23

Table IV. The desired and practical D-value of motion of the objective visual window with respect to the current (unit is mm).

No.	${}^{\text{abs}}\Delta px$	${}^{\text{abs}}\Delta py$	${}^{\text{abs}}\Delta pz$	${}^{\text{rel}}\Delta px$	${}^{\text{rel}}\Delta py$	${}^{\text{rel}}\Delta pz$
1	−61.4619	−31.1776	−40.1658	−61.4619	−31.1776	−40.1658
2	−132.0873	−1.2833	−33.0386	−132.0873	−1.2833	−33.0386
3	11.3638	−15.0398	61.6597	11.3638	−15.0398	61.6597

Table V. The link parameters for instrument arm 1.

k_1	k_2	k_3	θ_2	θ_3	θ_4	α	β	d_1	a_3	a_4	d_4	d_6	d_7	d_9	d_{10}	d_{11}	d_j
292	−292	−195	45°	45°	45°	45°	30°	1800	400	450	180	700	50	500	100	100	150

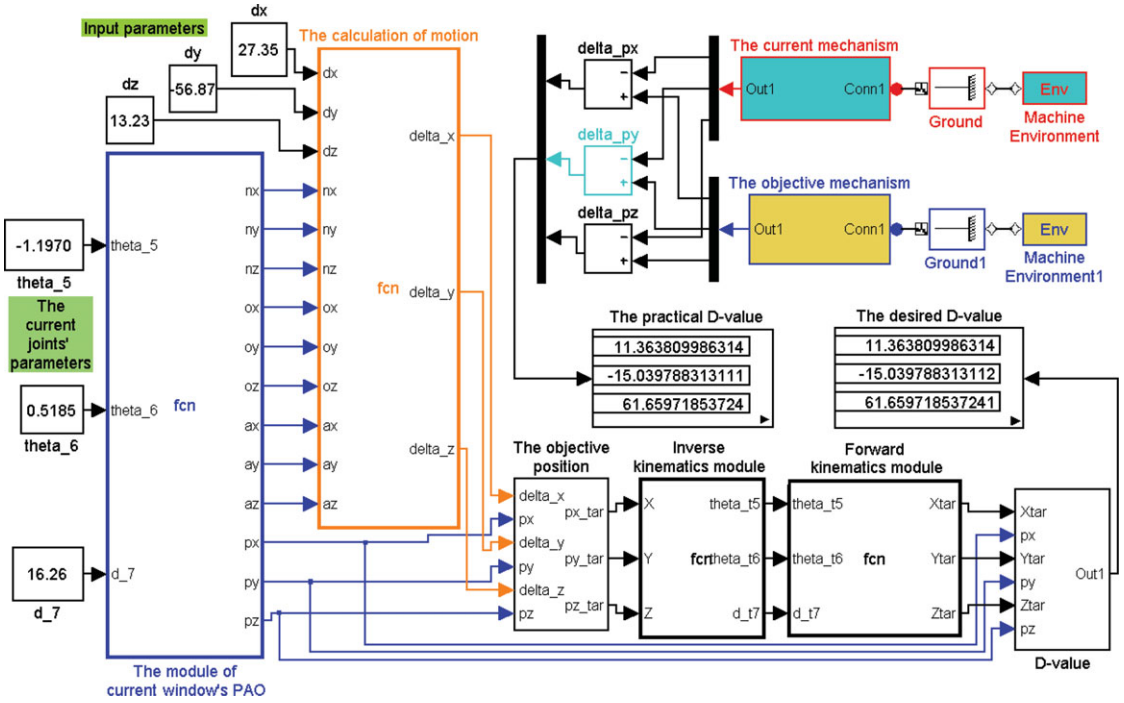


Fig. 9. (Colour online) The hybrid simulation model of the laparoscope arm's kinematics algorithm based on the DVW.

6.2.1. Kinematics simulation of the instrument arm 1. A group of constants is supposed to be the kinematics link parameters for the instrument arm 1, as shown in Table V, and the simulation model based on Simulink is set up as shown in Fig. 11. Three random digits created by the computer are chosen in the parameter scope of the active joints, which are input to the forward kinematics, the result is input to the inverse kinematics, and the outputs are θ_5, θ_6, θ_7, d_8, θ_9, θ_{10}. Therefore, the kinematics is corrected through a comparison of the input and output parameters and the numerical examples are shown in Table VI.

https://doi.org/10.1017/S026357471300088X Published online by Cambridge University Press

Table VI. The input and output parameters of instrument arm's simulation analysis.

No.	θ_5 (rad)	θ_6 (rad)	θ_7 (rad)	d_8 (mm)	θ_9(rad)	θ_{10} (rad)
1	1.4370	1.9840	−2.1510	27.85	1.4780	0.1473
2	1.4600	−0.5520	2.9570	38.56	1.4360	1.4370
3	1.4780	1.9600	0.0919	95.49	0.9434	−1.0760

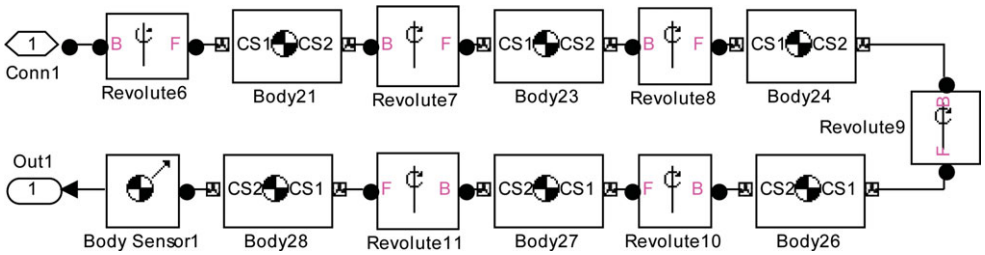


Fig. 10. (Colour online) The subsystem of the current and objective mechanisms in Fig. 9.

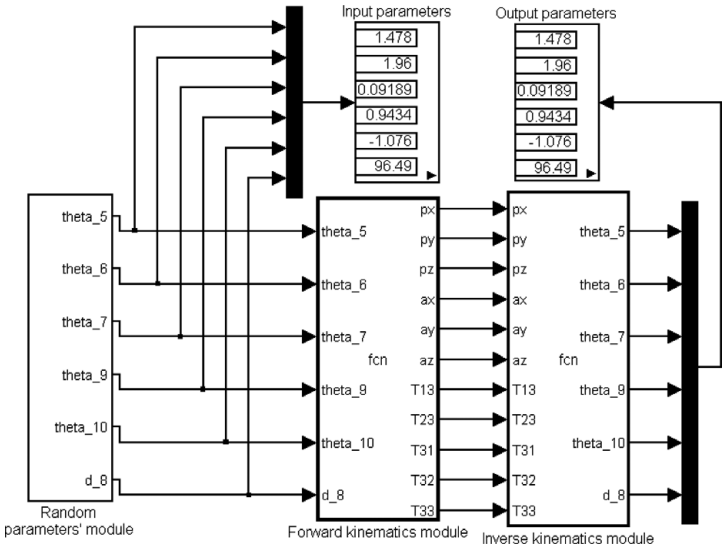


Fig. 11. The kinematics model of the Simulink simulation of instrument arm 1.

6.2.2. Hybrid simulation of the instrument arm's kinematics algorithm based on the DVW. Similar to Section 6.1.2, the hybrid simulation model is set up by the Simulink and SimMechanics toolboxes according to the instrument arm's kinematics algorithm based on the DVW, as shown in Fig. 12, and the subsystem of the current and objective mechanisms is shown in Fig. 13. The desired output is calculated by the Simulink model and the practical output comes from the SimMechanics model. The two outputs equally show the correctness of the instrument arm's kinematics algorithm based on the DVW.

As shown in Table VII, supposing matrix $\boldsymbol{T}_{\text{lap}}$ is the PAO of the current visual window and matrix ${}^{\text{dev}}_{\text{lap}}\boldsymbol{T}$ is the PAO of the instrument arm 1 based on the visual window, we use $(\psi, \phi, \varphi, {}_{\text{vis}}p_x, {}_{\text{vis}}p_y, {}_{\text{vis}}p_z)$ to describe it as in Section 5.2. We choose three groups of parameters as input to the simulation. Simultaneously, we use the parameters in Tables V–VII as inputs to the hybrid simulation model; the three groups of outputs are shown in Table VIII. The desired D-value of matrix $\Delta\boldsymbol{T}^{\text{dev}}_{\text{lap}}$ of the objective visual window based on the current is calculated from the Simulink model and the practical D-value of matrix $\Delta\boldsymbol{T}^{\text{dev}}_{\text{Bas}}$ is calculated from the SimMechanics model. The two outputs are the evidence to prove the correctness of the instrument arm's kinematics algorithm proposed in this research.

https://doi.org/10.1017/S026357471300088X Published online by Cambridge University Press

https://doi.org/10.1017/S026357471300088X Published online by Cambridge University Press

Table VII. The input parameters of the instrument arm's simulation analysis.

No.	$\boldsymbol{T}_{\text{lap}}$	${}^{\text{dev}}_{\text{lap}}\boldsymbol{T}$	$(\psi, \phi, \varphi, {}_{\text{vis}}p_x, {}_{\text{vis}}p_y, {}_{\text{vis}}p_z)$
1	$\begin{bmatrix} 0.7866 & -0.3892 & 0.4794 & -163.0442 \\ -0.7946 & 0.7062 & 0.7036 & 942.1271 \\ -0.6124 & -0.5915 & 0.5245 & 1380.1214 \\ 0 & 0 & 0 & 1.0000 \end{bmatrix}$	$\begin{bmatrix} 0.0593 & 0.3460 & -0.9364 & -50.0000 \\ -0.1632 & 0.9288 & 0.3328 & 70.0000 \\ 0.9848 & 0.1330 & 0.1116 & 30.0000 \\ 0 & 0 & 0 & 1.0000 \end{bmatrix}$	$(20^\circ, -30^\circ, 120^\circ, 50, -80, 150)$
2	$\begin{bmatrix} -0.0795 & 0.7036 & -0.7062 & 109.3830 \\ 0.7866 & 0.4794 & 0.3892 & 985.5492 \\ 0.6124 & -0.5245 & -0.5915 & 1632.9018 \\ 0 & 0 & 0 & 1.0000 \end{bmatrix}$	$\begin{bmatrix} -0.1112 & -0.4904 & 0.8643 & 650.0000 \\ 0.1330 & 0.8546 & 0.5020 & -370.0000 \\ -0.9848 & 0.1710 & -0.0301 & 240.0000 \\ 0 & 0 & 0 & 1.0000 \end{bmatrix}$	$(-50^\circ, 75^\circ, -130^\circ, -250, 380, 650)$
3	$\begin{bmatrix} 0.5597 & -0.0594 & 0.8265 & -339.9171 \\ -0.4365 & 0.8267 & 0.3550 & 965.6924 \\ -0.7044 & -0.5595 & 0.4368 & 1340.800 \\ 0 & 0 & 0 & 1.0000 \end{bmatrix}$	$\begin{bmatrix} 0.5567 & 0.0868 & 0.8262 & 130.0000 \\ -0.3214 & -0.8946 & 0.3105 & 221.0000 \\ 0.7660 & -0.4384 & -0.4701 & -123.0000 \\ 0 & 0 & 0 & 1.0000 \end{bmatrix}$	$(85^\circ, 133^\circ, 65^\circ, 123, 456, 789)$

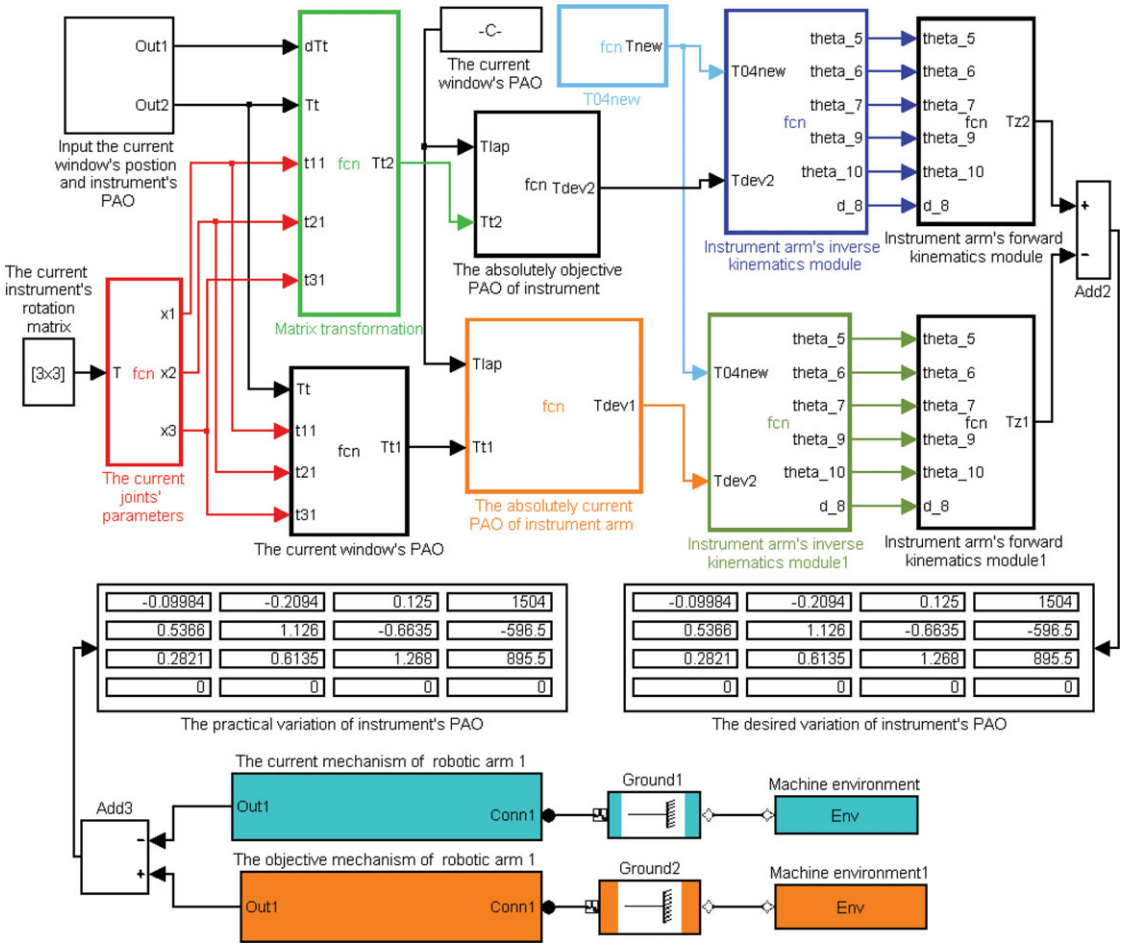


Fig. 12. (Colour online) The hybrid simulation model of the kinematics algorithm based on DVW for the instrument arm 1.

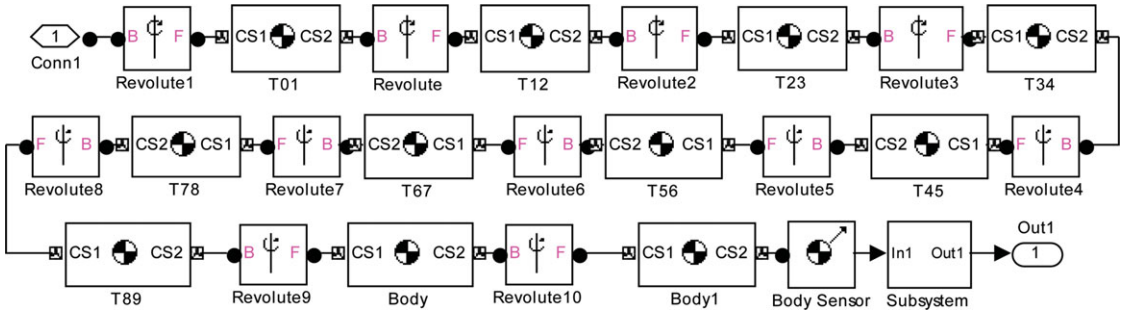


Fig. 13. (Colour online) The subsystem of the current and objective mechanisms in Fig. 12.

7. Conclusion

With the aim of enabling doctors to perform operations based on their visual and operation habits under the laparoscopic visual environment during the surgery, we propose a new kinematics method based on the DVW for the LSRS, and the problem of the consistency principle between the doctor's operations under the visual feedback of the visual window and the master–slave operations of the surgical robot is solved. First, the definition of the method for a 3D visual window is introduced and the approach of solving the method by kinematics is proposed. Second, we analyse the relations of the PAO among the normalized BCS, the objective and current visual window, in order to solve the laparoscope arm's kinematics algorithm based on the DVW; meanwhile, we analyse the relations of the PAO among the normalized BCS, the current visual window, and the objective and current

https://doi.org/10.1017/S026357471300088X Published online by Cambridge University Press

Table VIII. The desired and practical D-value of the objective PAO of instrument arm 1 based on the current.

No.	$\Delta \boldsymbol{T}_{\text{lap}}^{\text{dev}}$	$\Delta \boldsymbol{T}_{\text{Bas}}^{\text{dev}}$
1	$\begin{bmatrix} -0.6683 & 0.4095 & -0.1068 & 708.3000 \\ -0.5209 & -1.6420 & -0.7770 & 3.8860 \\ -1.5720 & 0.6102 & -0.376 & 80.3900 \\ 0 & 0 & 0 & 0 \end{bmatrix}$	$\begin{bmatrix} -0.6683 & 0.4095 & -0.1068 & 708.3000 \\ -0.5209 & -1.6420 & -0.7770 & 3.8860 \\ -1.5720 & 0.6102 & -0.376 & 80.3900 \\ 0 & 0 & 0 & 0 \end{bmatrix}$
2	$\begin{bmatrix} -1.1150 & -0.8094 & 0.5972 & -592.4000 \\ -0.3099 & -0.6416 & -1.337 & 3.6700 \\ 0.1774 & 0.0672 & -0.3168 & -627.4 \\ 0 & 0 & 0 & 0 \end{bmatrix}$	$\begin{bmatrix} -1.1150 & -0.8094 & 0.5972 & -592.4000 \\ -0.3099 & -0.6416 & -1.337 & 3.6700 \\ 0.1774 & 0.0672 & -0.3168 & -627.4 \\ 0 & 0 & 0 & 0 \end{bmatrix}$
3	$\begin{bmatrix} -0.0998 & -0.2094 & 0.1250 & 1504.0000 \\ 0.5366 & 1.1260 & -0.6635 & -596.5000 \\ 0.2821 & 0.6135 & 1.2680 & 895.5000 \\ 0 & 0 & 0 & 0 \end{bmatrix}$	$\begin{bmatrix} -0.0998 & -0.2094 & 0.1250 & 1504.0000 \\ 0.5366 & 1.1260 & -0.6635 & -596.5000 \\ 0.2821 & 0.6135 & 1.2680 & 895.5000 \\ 0 & 0 & 0 & 0 \end{bmatrix}$

end-effector's TCS, to solve the instrument arms' kinematics algorithm based on the DVW. Third, the kinematics algorithms based on the DVW with respect to the kinematics models of the LSRS and the relative coordinate transformations are established. Finally, the Simulink model for the forward and inverse kinematics is established and the correctness is verified through three groups of random constant parameters created by the computer. The hybrid simulation models for the new kinematics algorithms based on the Simulink and SimMechanics toolboxes of MATLAB are set up. According to the three groups of the numerical experimentation for the laparoscope and instrument arms, the desired PAO is calculated by the Simulink model and the practical PAO is calculated by the SimMechanics model. The two outputs equally show the correctness and the feasibility of the new kinematics algorithm based on the DVW. This kinematics method can be the specialized kinematics algorithms for this kind of a surgical robot system and other applicative robotics industry with the visual feedback and the master–slave control.

Future work will focus on verifying the kinematics algorithms based on the DVW through the practical experiment system of the LSRS and performing relevant verification experiments during the doctors' surgical operations, in order to improve the kinematics method proposed in this research.

Acknowledgements

This work is partially supported by the National Natural Science Foundation of China (grant 61203358/F0306), the Research Fund for the Doctoral Program of Higher Education of China (grant 20102304120006), the State Key Laboratory of Robotics and System (HIT) (grant SKLRS-2010-MS-04), the Fundamental Research Funds for the Central Universities (grant HEUCFZ1214), and the Special Fund for Outstanding Talented Person of Harbin City (grant 2012RFQXS067).

References

1. G. T. Sunga and I. S. Gill, "Robotic laparoscopic surgery: A comparison of the da Vinci and Zeus systems," *Urology* **58**(6), 893–898 (2001).
2. R. Valero, Y. H. Ko, S. Chauhan, O. Schatloff, A. Sivaraman, R. F. Coelho, F. Ortega, K. J. Palmer, R. Sanchez-Salas, H. Davila, X. Cathelineau and V. R. Patel, "Robotic surgery: History and teaching impact," *Actas Urol. Esp*. **35**(9), 540–545 (2011).
3. T. Haidegger and Z. Benyo, "Surgical robotic support for long duration space missions," *Acta Astronaut*. **63**(7–10), 996–1005 (2008).
4. N. Monsarrat, P. Collinet, F. Narducci, E. Leblanc and D. Vinatier, "Robotic assistance in gynaecological surgery: State-of-the-art," *Gynécol. Obstét. Fertil.* **37**(5), 415–424 (2009).
5. T. Giuseppe, P. Ilaria, P. Francesca and C. Alfred, "Economic evaluation of da Vinci-assisted robotic surgery: A systematic review," *Surg. Endosc*. **26**(3), 598–606 (2012).
6. U. Hagn, M. Nickl, S. Jörg, G. Passig, T. Bahls, A. Nothhelfer, F. Hacker, L. Le-Tien, A. Albu-Schäffer, R. Konietschke, M. Grebenstein, R. Warpup, R. Haslinger, M. Frommberger and G. Hirzinger, "The DLR MIRO: a versatile lightweight robot for surgical applications," *Ind. Robot: Int. J*. **35**(4), 324–336 (2008).

https://doi.org/10.1017/S026357471300088X Published online by Cambridge University Press

7. R. Konietschke, U. Hagn, M. Nickl, S. Jörg, A. Tobergte, G. Passig, U. Seibold, L. Le-Tien, B. Kübler, M. Gröger, F. Fröhlich, C. Rink, A. Albu-Schäffer, M. Grebenstein, T. Ortmaier and G. Hirzinger, "The DLR MiroSurge: A Robotic System for Surgery," **In**: *2009 IEEE International Conference on Robotics and Automation*, Kobe, Japan (May 12–17, 2009) pp. 1589–1590.
8. M. J. H. Lum, D. C. W. Friedman, G. Sankaranarayanan, H. King, K. Fodero, B. Hannaford, J. Rosen and M. N. Sinanan, "The RAVEN: Design and validation of a telesurgery system," *Int. J. Robot. Res*. **28**(9), 1183–1197 (2009).
9. R. Jacob, L. Mitchell, S. Mika and H. Blake, "Raven: Developing a Surgical Robot from a Concept to a Transatlantic Teleoperation Experiment," **In**: *Surgical Robotics: Systems Applications and Visions* (J. Rosen, B. Hannaford and R. M. Satava, eds.), (Springer, New York, US, 2011) pp. 159–197.
10. T. Hornyak, 2010. Paging Raven II: the open-source surgery robot. CNET [internet]. Available at: http://news.cnet.com/8301-17938_105-573624501/paging-raven-ii-the-open-source-surgery-robot/.
11. L. van den Bedema, N. Rosiellea and M. Steinbuch, "Design of Slave Robot for Laparoscopic and Thoracoscopic Surgery," *20th International Conference of Society for Medical Innovation and Technology*, Vienna, Austria (August 28–30, 2008).
12. P. Berkelman and J. Ma, "A compact modular teleoperated robotic system for laparoscopic surgery," *Int. J. Robot. Res*. **28**(9), 1198–1215 (2009).
13. O. Weede, H. Mönnich, B. Müller and H. Wörn, "An Intelligent and Autonomous Endoscopic Guidance System for Minimally Invasive Surgery," *2011 IEEE International Conference on Robotics and Automation,* Shanghai, China (May 9–13, 2011) pp. 5762–5768.
14. C. Staub, C. Lenz, G. Panin, A. Knoll and R. Bauernschmitt, "Contour-Based Surgical Instrument Tracking Supported by Kinematic Prediction," *Proceedings of the 2010 3rd IEEE RAS and EMBS*, Tokyo, Japan (September 26–29, 2010) pp. 746–752.
15. S. Tully, G. Kantor, M. A. Zenati and H. Choset, "Shape Estimation for Image-Guided Surgery with a Highly Articulated Snake Robot," *2011 IEEE/RSJ International Conference on Intelligent Robots and Systems, San Francisco*, CA, USA (September 25–30, 2011) pp.1353–1358.
16. B. Gherman, D. Pislan, C. Vaida and N. Plitea, "Development of inverse dynamic model for a surgical hybrid parallel robot with equivalent lumped masses," *Robot. Comput.-Integr. Manuf.* **28**(3), 402–415 (2012).
17. O. R. Brouwer, T. Buckle, A. Bunschoten, J. Kuil, A. L. Vahrmeijer, T. Wendler, R. A. Valdés-Olmos, H. G. van der Poel and F. W. B. van Leeuwen, "Image navigation as a means to expand the boundaries of fluorescence-guided surgery," *Phys. Med. Biol*. **57**(10), 3123–3136 (2012).

https://doi.org/10.1017/S026357471300088X Published online by Cambridge University Press